Title

A Finite Element Analysis-Based Study of Mechanical Behavior of Nanoporous Gold Thin Films on Silicone Substrates with Varying Effective Stiffness

Permalink

https://escholarship.org/uc/item/59c9748v

Author

Somayajula, Kavya Geetika

Publication Date

2024

Peer reviewed|Thesis/dissertation

A Finite Element Analysis-Based Study of Mechanical Behavior of Nanoporous Gold
Thin Films on Silicone Substrates with Varying Effective Stiffness

By

KAVYA GEETIKA SOMAYAJULA

THESIS

Submitted in partial satisfaction of the requirements for the degree of

MASTER OF SCIENCE

in

Mechanical and Aerospace Engineering

in the

OFFICE OF GRADUATE STUDIES

of the

UNIVERSITY OF CALIFORNIA

DAVIS

Approved:

_____
Erkin Şeker, Chair

_____
Jeremy Mason

_____
Barbara S. Linke

Committee in Charge

2024

ABSTRACT

Nanostructured materials offer tremendous opportunities for engineering advanced device components for diagnostic and therapeutic applications. One such material, nanoporous gold (np-Au), has found use in applications ranging from catalysis to biosensing, where pore morphology plays a critical role in performance. Np-Au is typically produced by a process known as dealloying, where immersion in nitric acid selectively removes silver from a gold-silver alloy and gold surface atoms diffuse at the metal-electrolyte interface arranging into a bicontinuous ligament network. While morphology evolution of bulk np-Au has been widely studied, knowledge about its thin film form, which is influenced by the underlying substrate, is limited. This thesis delves into the mechanical behavior of nanoporous gold (np-Au) thin films on substrates of varying mechanical compliance, focusing on the role of substrate stiffness controlled by the thickness of polydimethylsiloxane (PDMS) layers anchored onto a rigid glass slide. Using a finite element analysis (FEA) framework, the study simulates the deformation and strain energy characteristics of np-Au films, revealing a nuanced interplay between substrate compliance and film morphology. Simulation results indicate that the effective elastic modulus of PDMS, modulated by its thickness, critically affects the deformation patterns in np-Au thin films. At the film-substrate interface, simulations show that the np-Au/PDMS system undergoes significantly greater deformation than np-Au/glass, characterized by both in-plane compressive and out-of-plane vertical displacements. The study further presents a detailed analysis of strain energies, with the simulations uncovering that the total strain energy of the film-PDMS system decreases as PDMS thickness increases. Corresponding experiments performed in our group show that the decrease in strain energy is associated with the diminished presence of macroscopic cracks in the np-Au films on thicker PDMS substrates from experiments, as opposed to those on glass. The simulations also highlight that the distribution and intensity of microscopic cracks are contingent on the PDMS thickness, confirming experimental observations of the hierarchical crack formation in the np-Au/PDMS

system and offering predictive insights into the mechanical stability of the films. In conclusion, the simulations provide compelling evidence that the mechanical characteristics of np-Au films can be finely tuned by adjusting the thickness of the anchored compliant substrate. This paves the way for engineering advanced materials with tailored morphological properties, optimizing np-Au thin films for applications in flexible electronics and wearable sensors.

Acknowledgements

As I reflect on the journey that has led to the completion of this thesis, my heart is filled with gratitude for those who have supported me along the way.

First and foremost, I would like to extend my sincere thanks to Prof. Erkin Şeker for his continuous mentorship and invaluable advice throughout this process. His expertise and encouragement have provided me with an unparalleled learning experience, for which I am immensely grateful. I am also thankful for Sadi Shahriar, whose contributions of experimental results and companionship have been invaluable. Working alongside Sadi has not only been academically enriching but also a great deal of fun, adding a unique and enjoyable dimension to my research experience. Special mention to my committee members, Prof. Jeremy Mason, for his critical insights that were crucial in refining my thesis, and Prof. Barbara Linke, for her feedback that enhanced my work.

My deepest gratitude goes out to my family back in India - my parents and sister, whose unwavering support and love have been my foundation. Despite the physical distance, their belief in me has been a constant source of strength and motivation. Their sacrifices and encouragement have shaped me into the person I am today, and I owe them everything.

Lastly, I must acknowledge my friends in Davis, who have become like family to me. They have made my master's journey truly memorable, providing not only a sense of home away from home but also endless moments of joy and solace. Their support and camaraderie have been indispensable, making every challenge more manageable and every success sweeter.

To all who have contributed to my journey and this thesis, directly or indirectly, I offer my heartfelt thanks. This accomplishment is not just my own but a testament to the collective support, guidance, and encouragement I have been fortunate enough to receive.

Table of Contents

List of Figures

List of Tables

List of Abbreviations

1. np-Au - Nanoporous gold

2. FEA - Finite Element Analysis

3. SEM - Scanning Electron Microscope

4. PV - Photo Voltaic

5. PVD - Physical Vapor Deposition

6. CVD - Chemical Vapor Deposition

7. LPCVD - Low Pressure Chemical Vapor Deposition

8. PECVD - Plasma Enhanced Chemical Vapor Deposition

9. MOCVD - Metal Oxide Chemical Vapor Deposition

10. CTE - Coefficient of Thermal Expansion

11. MD - Molecular Dynamics

12. DFT - Density Functional Theory

13. AFM - Atomic Force Microscope

14. AuAg – Gold silver alloy

15. Cr – Chromium

16. Au - Gold

1. INTRODUCTION

1.1 Thin films, fabrication and characterization methods, and applications

A thin film is a layer of material that can vary in thickness from a fraction of a nanometer (atomic monolayer) to several micrometers. In recent times, the ability to customize the characteristics of a film by adjusting the microstructure through specific deposition parameters has enabled its use in a wide range of applications, from basic protective coatings against wear and corrosion to highly advanced fields like microelectronics and biomedicine [1]. Thin films and coatings are widely used in various industries, including optics, advanced optoelectronic devices [2], the photovoltaic sector (PV) [3], and biomedical applications [4], with applications such as invasive medical devices [5-6], tissue engineering substrates [7], drug delivery systems [8-9], and antimicrobial coatings [10]. The diverse range of thin films to enable specific applications require certain morphological, mechanical, and chemical features that are closely connected to the deposition procedures and process parameters employed.

The main categories of deposition techniques for thin films are physical vapor deposition (PVD) and chemical vapor deposition (CVD) [11]. The key differentiating factor between PVD and CVD is the composition of the vapor. In physical vapor deposition, the vapor consists of atoms and molecules that condense directly onto the substrate. On the other hand, in chemical vapor deposition, the vapor undergoes a chemical reaction within itself or with the substrate, leading to the formation of a thin film. The two fundamental types of PVD are thermal evaporation [12], and sputtering [13]. Chemical vapor deposition can be classified based on the variations based on pressure conditions, physical vapor characteristics, substrate heating methods and plasma processing. Most common CVD techniques include low-pressure CVD (LPCVD), plasma enhanced CVD (PECVD) and metal organic CVD (MOCVD). LPCVD is ideal for minimizing unwanted gas-phase reactions and improving film uniformity at sub-atmospheric pressures [14], whereas PECVD accelerates chemical reactions with plasma, enabling lower temperature

depositions suitable for semiconductors and organic coatings [15]. Metalorganic CVD (MOCVD) employs metalorganic precursors to produce compound semiconductors and a variety of nanomaterials [16]. Challenges remain in attaining cost-efficiency, reproducibility, thin film adhesion onto surfaces, reduced temperature, and control of thin film properties.

1.2 Mechanical Behavior of Thin films

The mechanical properties of thin films are different from those of bulk materials because of their unique microstructure, large surface-to-volume ratio, reduced dimensions, and the constraints caused by the substrate [17]. Understanding the mechanical properties of thin films on substrates requires an understanding of the stresses in thin film structures as well as a knowledge of the mechanisms by which thin films deform [18]. A stress may be induced in a film by the application of external forces to the film-substrate system. Any modulus mismatch between the film and substrate will result in a discontinuity in the stresses parallel to the interface. In addition to stresses induced by external loads, residual stresses often emerge during and after fabrication of the film [19]. Residual stress in thin films may be originate from a variety of reasons, including (1) thermal stress resulting from the difference in coefficients of thermal expansion (CTE) of thin film and substrate; (2) interfacial stress largely caused by the difference in the lattice structural properties between thin film and substrate, and (3) intrinsic stress in thin films induced during deposition or post deposition treatment (e.g., annealing).

1.3 Mechanical Behavior of Thin films on different substrates

Thin film deposition is usually done at fairly high temperatures, with PVD processes such as sputtering and evaporation usually operating within the range of room temperature to approximately 500°C [13]. In PVD processes, the conversion of the target material into a vapor phase for deposition does not necessarily require the substrate to be heated, as the energy for this phase change primarily comes from the source. However, substrates may be intentionally heated to improve film adhesion, crystallinity, and to control the microstructure of the deposited

film, enhancing its physical and chemical properties. On the other hand, CVD processes often require temperatures in the range of 100°C to over 1000°C [20], as these processes intrinsically involve high temperatures to supply thermal energy to the chemical reactions that result in thin film deposition onto the substrate. The substrate is usually heated to a specific temperature range that facilitates the desired chemical reactions between the gas-phase precursors, leading to the formation of a solid film. Controlled cooling following thin film deposition is crucial to manage thermal stresses [21], influence phase and microstructure evolution [22], maintain film-substrate interface quality [23], and achieve desired material properties. This change in temperature and the difference in CTEs result in residual stresses, where the thin film must be able to tolerate residual stresses without fracture or delamination from the substrate to satisfy requirements for intended application [8]. Different substrates, such as metals, plastics, and ceramics, have significant impacts on the thin film and substrate's mechanical behavior. The mechanical properties of the substrate directly affect how the thin film deforms and the stress distribution within the film. The thin film is less likely to deform when placed on a stiff substrate, increasing the concentration of stress at interfaces and increasing the risk of cracking or delamination. Compliant substrates, on the other hand, permit greater deformation which may result in stress relaxation and a decrease in mechanical stress in the film; however, this may result in other types of deformations (e.g., buckling). If the substrate is considerably stiffer than the film, the fractures may only extend partially through the film [9], but when the substrate is more compliant than the film, the cracks may extend through the film to the substrate and delaminate at the film-substrate interface [10].

1.4 Nanoporous gold

While thin films encompass a wide range of materials with applications across various domains, metal thin films have garnered significant attention for their electrical, thermal, and optical properties. These films can be broadly categorized into dense metal thin films and porous metal

thin films, each exhibiting distinct characteristics and functionalities derived from their unique morphologies. Solid metal thin films are characterized by their dense, uniform structures and are integral to the fabrication of electronic devices requiring electrically conductive paths [25-26], protective coatings [27-28], and functional layers in sensors and circuits [28]. In contrast, porous metal thin films are distinguished by their intricate network of pores. The porosity of these films can be carefully controlled to optimize their properties for specific applications, including bio-sensing, drug delivery, and electrochemical devices.

Among many porous metal films, nanoporous gold (np-Au) distinguishes itself with its unique structure. Characterized by its 10s of nanometer-scale interconnected ligaments and highly tunable porous architecture, np-Au merges the advantageous traits of metal films with the added benefits of a high surface area, making it an exceptional material for advanced applications in catalysis, electronics, and biomaterials [7-8]. Np-Au is fabricated by a process called dealloying. The dealloying process for gold-silver (AuAg) alloys, which are composed of 60–80 atomic% Ag, involves the selective dissolution of Ag atoms, while gold atoms diffuse at the metal-electrolyte interface. This results in the formation of a bicontinuous ligament and pore structure, consisting predominantly of Au atoms [31]. The thin film forms of nanoporous metals enable their integration into functional devices (e.g., sensors) via conventional photolithographic techniques [32]. However, thin films supported by an underlying substrate often exhibit residual stresses as mentioned above. Compressive residual stress can cause delamination in blanket films and lead to buckling in freestanding structures, while tensile stress primarily contributes to cracking and is a significant factor in some cases of delamination [29]. To enhance adhesion of AuAg films to silicon or glass, a foundational layer of chrome and gold is essential, where absence of these layers and residual stress from volume contraction are primary reasons for delamination during dealloying. Techniques such as nanoindentation, tensile testing, wafer curvature measurement methods are employed to measure the residual stresses and the material's mechanical

4

properties, including its Young's modulus, yield strength, and plasticity. These measurements are crucial for predicting the material's behavior under load, its resilience, and its suitability for various applications. Additionally, advanced microscopy and spectroscopy techniques play an essential role in correlating the material's morphology and surface chemistry with its mechanical properties, providing a comprehensive understanding of how nano-scale features contribute to macro-scale behavior. Building on the foundation laid by experimental characterization, computational techniques, particularly finite element analysis (FEA), offer a powerful approach for further understanding and predicting the complex behavior of np-Au films under various conditions, bridging the gap between nano-scale features and their macro-scale mechanical properties.

1.5 FEA and thin films

Finite element analysis (FEA) is a numerical technique used to obtain an approximate solution for problems involving an elliptical partial differential equation with boundary conditions by dividing the whole domain into number of finite elements as per the problem [33]. The application of FEA has been implemented into static structural problems, steady-state thermal, hydrodynamic problems, magnetostatic analysis, eigen-value problems, fluid flow problems, etc. FEA's strength lies in its ability to handle complex geometries and material behaviors under different loading and boundary conditions, making it essential for designing and optimizing thin film applications. While FEA stands as a cornerstone for predicting and optimizing the behavior of thin films under various conditions, it is not without its complexities. The intricacy of simulating thin film phenomena stems from factors such as mesh sensitivity, material property characterization, and the accurate representation of boundary conditions. Moreover, the multifaceted nature of thin films necessitates advanced computational strategies to tackle issues like multi-physics coupling and scale bridging, highlighting the ongoing quest for enhanced simulation accuracy and efficiency.

Beyond FEA, several computational techniques such as molecular dynamics (MD) play a pivotal role in the characterization of thin films, each with its unique strengths and applications. MD

simulations delve into atomic-scale interactions, offering insights into the fundamental mechanisms that show how molecular/atomic systems move over time [34]. Density functional theory (DFT) provides a quantum mechanical description of a material's electronic structure, essential for understanding its mechanical properties from an atomic perspective. Monte Carlo simulations offer probabilistic insights into material equilibrium properties, for example, potential energy calculations, absorption studies, phase equilibria studies [11]. While each of these techniques have their merits, since MD simulations provide atomic-level insights, they might be more suitable for understanding material behavior such as thermal conductivity, viscosity, and diffusivity coefficients, whereas FEA can be used for practical engineering applications.

1.6 Objectives of the thesis

Despite research on deformation and cracking behavior of metal thin films on compliant substrates [13], there is little information on how substrate compliance influences the mechanical characteristics of nanoporous metal thin films made by dealloying. This thesis examines the mechanical characteristics, including strain energy and deformations, of np-Au thin films that are deposited on polydimethylsiloxane (PDMS) "silicone" substrates with different thicknesses and anchored to an underlying rigid substrate. The "effective elastic modulus" of the substrate that the np-Au thin film experiences is modulated in this system by varying the thickness of the compliant silicone layer. In addition, the strains and deformations are compared in the both as-deposited AuAg and post dealloyed np-Au films on the compliant substrates to those of the films on the rigid substrate that has a much higher stiffness.

2. METHODOLOGY AND EQUATIONS

2.1 Experimental setup

In order to put the simulations in context, it is important to briefly mention the accompanying experiments. For the fabrication of np-Au films, the preliminary step involved the cleaning of glass slides with isopropanol, followed by drying with a nitrogen gun before attaching the PDMS layers of thicknesses (0.25, 0.50, 1.59, and 3.18 mm). The PDMS and glass were then subjected to an air plasma treatment to promote covalent bonding upon joining. The deposition process for the AuAg alloy films entailed a tiered approach: starting with a chromium adhesion layer (Cr) (~160nm-thick), followed by a gold intermediary (Au) (~80 nm-thick), and concluded with an $Au_{0.24}Ag_{0.76}$ (atomic%) alloy layer (~600 nm-thick) alloy layer. This methodical layering was essential for the integrity of the final np-Au films, which were produced by dealloying the AuAg precursor in 70% nitric acid at 55°C for 15 minutes, followed by rinsing in deionized water and drying under nitrogen flow.

2.2 Simulation setup

Finite element analysis (FEA) simulations were performed using COMSOL Multiphysics software (Version 6.0), as described in the Appendix. These involved simulating the mechanical behavior of np-Au thin films on a compliant PDMS substrate with the PDMS fixed at the bottom to mimic the rigid glass substrate. Simulations were performed to estimate (a) the effective elastic modulus of PDMS of variable thickness anchored to a glass substrate, (b) the dependence of the strain energy of the thin film layers and the PDMS substrates after deposition and dealloying, and (c) average horizontal and vertical edge deformation magnitude at the PDMS-metal stack interface, all as a function of PDMS thickness. The strain energy and deformation simulations involve AuAg/Au/Cr layers for the *post-deposition* and np-Au/Au/Cr layers for the *post-dealloying* conditions with the PDMS substrates fixed at the bottom to mimic being anchored to rigid glass slides experimentally.

2.2.1 Effective elastic modulus calculations

The first set of simulations was performed in two dimensions (2D) to calculate the "effective elastic modulus" E_P of the anchored PDMS substrates wherein the PDMS was 5 mm in both length and width with the thickness 0.01, 0.10, 0.15, 0.25, 0.50, 1.59, 3.18 and 5 mm. A tetrahedral mesh with an element size range of 0.501 µm to 2.5 µm was used for this set of simulations. To estimate the effective surface modulus E_P, two points on the top surface of PDMS as shown in **Figure 1** were displaced axially in the x-direction by the application of a force $f = 0.0001$ N per unit depth. The initial separation distance between two such points on the PDMS was fixed at 200 µm.
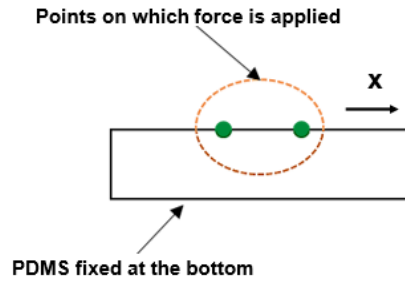

Figure 1: Schematic showing the simulation setup to compute the effective elastic modulus of PDMS at the surface.

The effective elastic modulus E_P was defined by equating the average strain energy density within the PDMS to that of a linear elastic isotropic solid under uniform strain. The change in the separation of the contact points was written as $(w - w_0)$ and the initial volume of PDMS per unit depth between the contact points was given by $h_p w_0$, leading to a strain energy density of $f(w - w_0)/(h_p w_0) = f\varepsilon/h_P$ where $\varepsilon = (w - w_0)/w_0$ denotes the linear strain experienced at the PDMS surface. By equating this strain energy density to the elastic strain energy $E_P \varepsilon^2/2$ of an isotropic linear elastic solid, the Young's modulus E_P as a function of the PDMS thickness h_P can be calculated by the formula:

$$E_P = \frac{2f}{h_P \varepsilon} \tag{1}$$

Equation (1) estimates the Young's modulus relative to the PDMS thickness which is instrumental in understanding the mechanical properties of the substrate and is pivotal for the design considerations in microscale applications.

2.2.2 Strain energy and deformation simulations

The second set of simulations was performed to estimate the elastic strain energy in the thin film-substrate system, and the horizontal and vertical edge displacements at the metal film/substrate interface before and after dealloying. The PDMS layer was 2.5 mm in both length and width for these simulations with thickness of 0.05, 0.10, 0.15, 0.25, 0.50, 0.75, 1, 1.59, 3.18, and 5 mm. The thicknesses of the AuAg (post-deposition) and np-Au (post-dealloying) films were 600 nm and 500 nm (reduction due to volume contraction that typically occur during dealloying [35]), respectively, and the Cr and Au adhesion layers had thicknesses of 160 nm and 80 nm, respectively. A free quadrilateral element mesh with an element size range of 0.079 μm to 318 μm was used. A swept mesh was applied for all the layers (shown in **Figure 2**), with the number of elements through the thicknesses of AuAg and np-Au films, adhesion layers, and PDMS indicated in **Table 1**. While tetrahedral meshes have their own advantages, since the geometry here was a regular, prismatic shape, swept meshes are highly efficient. Specifically, swept meshes also require fewer elements to fill up the volume than tetrahedral meshes, leading to fewer degrees of freedom and in turn reducing the computational demand. Every thin film layer was ensured to have a sufficient number of elements through the thickness to accurately capture the stress gradients.

Table 1: Geometry and mesh information for strain energy and deformation simulations

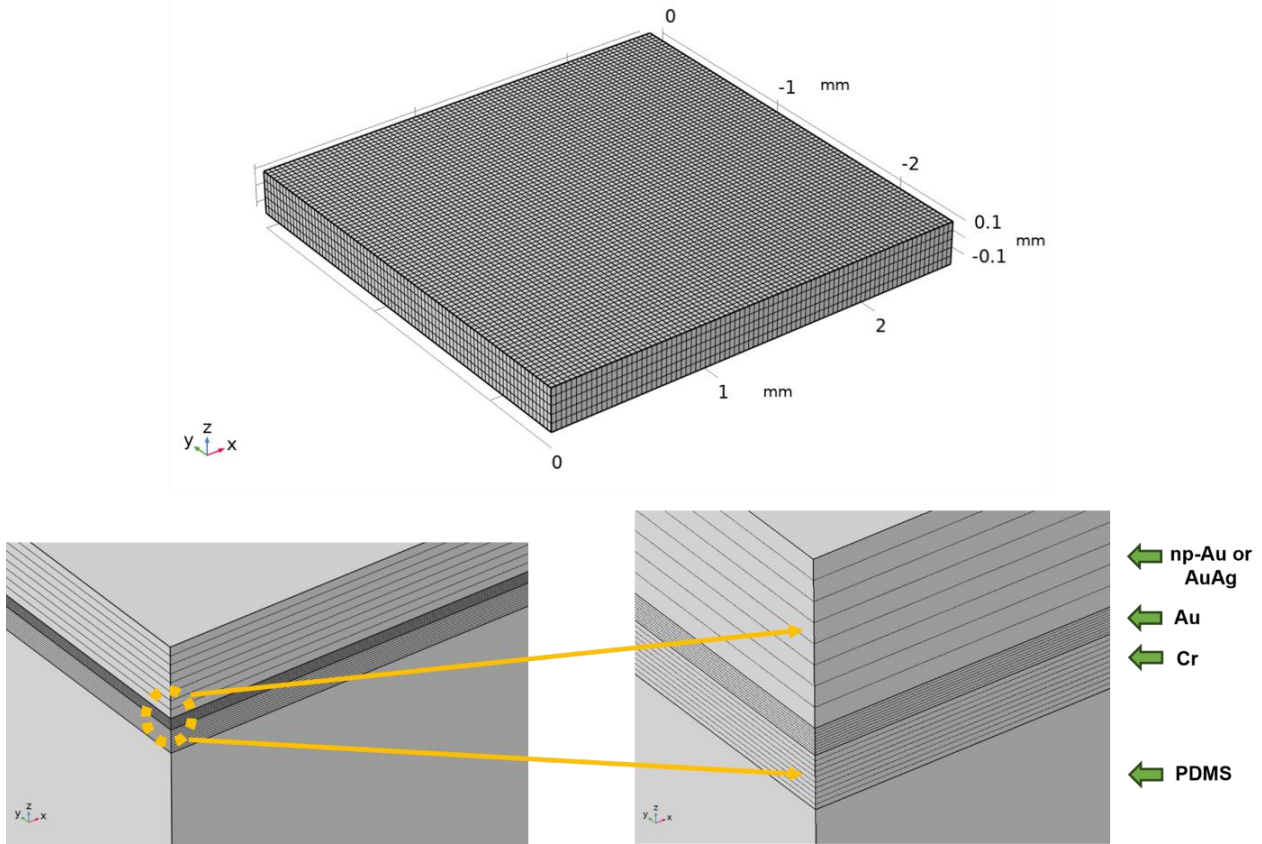|	*Mesh Type*	*No of elements along thickness*	*Layer thickness*
AuAg film	Free quad	8	500nm
Adhesion layers	Free quad	10	Cr thickness = 160nm Au thickness = 80nm
PDMS	Free quad	>5	0.05, 0.10, 0.15, 0.25, 0.50, 0.75, 1, 1.59, 3.18, and 5 mm

Figure 2: Finite element mesh for the post-deposition and post-dealloying film/substrate stack.

The experimentally-obtained residual stress value of ~100 MPa was used to estimate the thermal strain experienced by the AuAg, Au, and Cr films following deposition [7,13]. The thermal strain was calculated using the following equations (2) and (3), where ϵ_{th} stands for thermal strain, σ is

the thermal stress, E is the Young's modulus, α is the coefficient of thermal expansion (CTE) and $(T - T_{ref})$ is the temperature difference, with T_{ref} being the reference temperature.

$$\epsilon_{th} = \frac{\sigma}{E} \tag{2}$$

$$\epsilon_{th} = \alpha(T - T_{ref}) \tag{3}$$

The corresponding thermal strain was translated into a temperature difference using the CTE of the film and fed into the software as the thermal contraction condition. The thermal strain calculated based on the temperature difference leads to a stress in the software by offsetting the elastic strain according to the following constitutive law:

$$\sigma = C : (\varepsilon - \varepsilon_{th}) \tag{4}$$

where ε_{th} is the thermal strain that accounts for the volume change associated with the temperature variation. All the materials used in the simulations are considered as linear elastic materials with the material properties (including the CTEs used in these simulations) listed in **Table 2**.

Table 2: Material properties of materials used in the simulation.

Properties	As-deposited AuAg	Dealloyed np-Au	PDMS	Chromium (Cr)	Gold (Au)
Young's modulus	77 GPa	20 GPa	1 MPa[37]	279 GPa[38]	79 GPa[39]
Poisson's ratio	0.3	0.3	0.4	0.2	0.3
Coefficient of thermal expansion	10^{-5} / °C	10^{-5} / °C	0	3.3×10^{-6} / °C	10^{-5} / °C

3. RESULTS AND DISCUSSION

Here, the simulation results are presented in relation to experimental results (performed by Sadi Shahriar) to facilitate the discussion. **Figure 3** depicts the deformation along the horizontal and vertical axes at the film-substrate boundary as derived from simulation data. As illustrated in **Figure 4**, the deformation observed at the np-Au/glass interface post-dealloying is notably minimal, while on the other hand, the np-Au/PDMS interface experiences significantly greater deformation, exhibiting both in-plane (horizontal) and out-of-plane (vertical) contractions. For the post-deposition case, the mean horizontal displacement at the np-Au/PDMS boundary increases from 1.07 μm for PDMS with a 0.05 mm thickness to 1.12 μm for PDMS at 5 mm thickness (**Figure 3a**), while the mean vertical displacement (**Figure 3b**) increases from 0.69 μm at 0.05 mm-thick PDMS to 0.94 μm at 3.18 mm-thick PDMS. Moreover, the average horizontal and vertical displacements at the AuAg/PDMS interface, recorded post-deposition, are observed to be slightly higher than those post-dealloying for PDMS at all considered thicknesses, which is attributed to the reduced effective elastic modulus of porous thin film (i.e., np-Au) compared to its dense counterpart (i.e., AuAg).
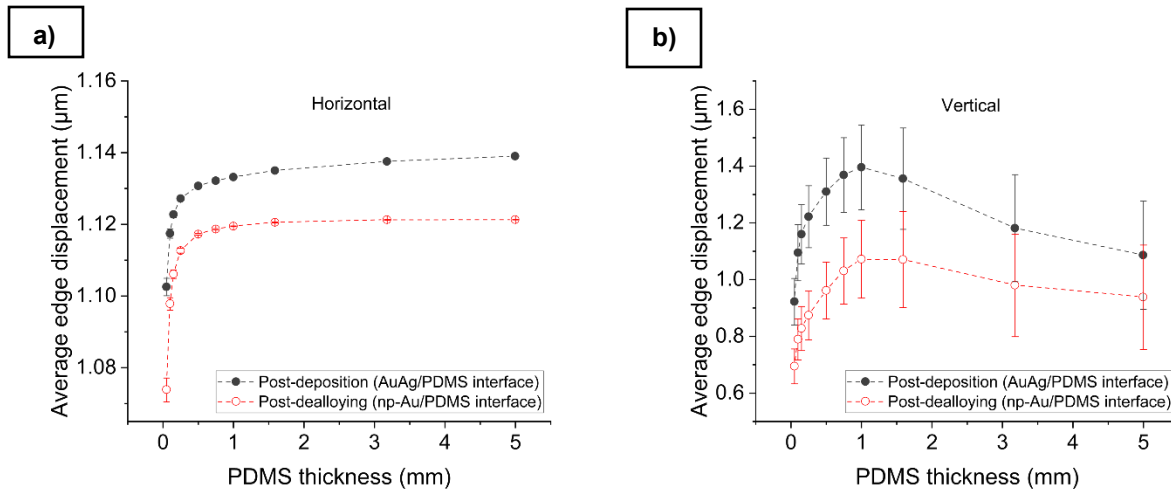

Figure 3: Average (a) horizontal and (b) vertical post-deposition and post-dealloying edge displacements at the AuAg/PDMS with respect to the non-deformed structure.
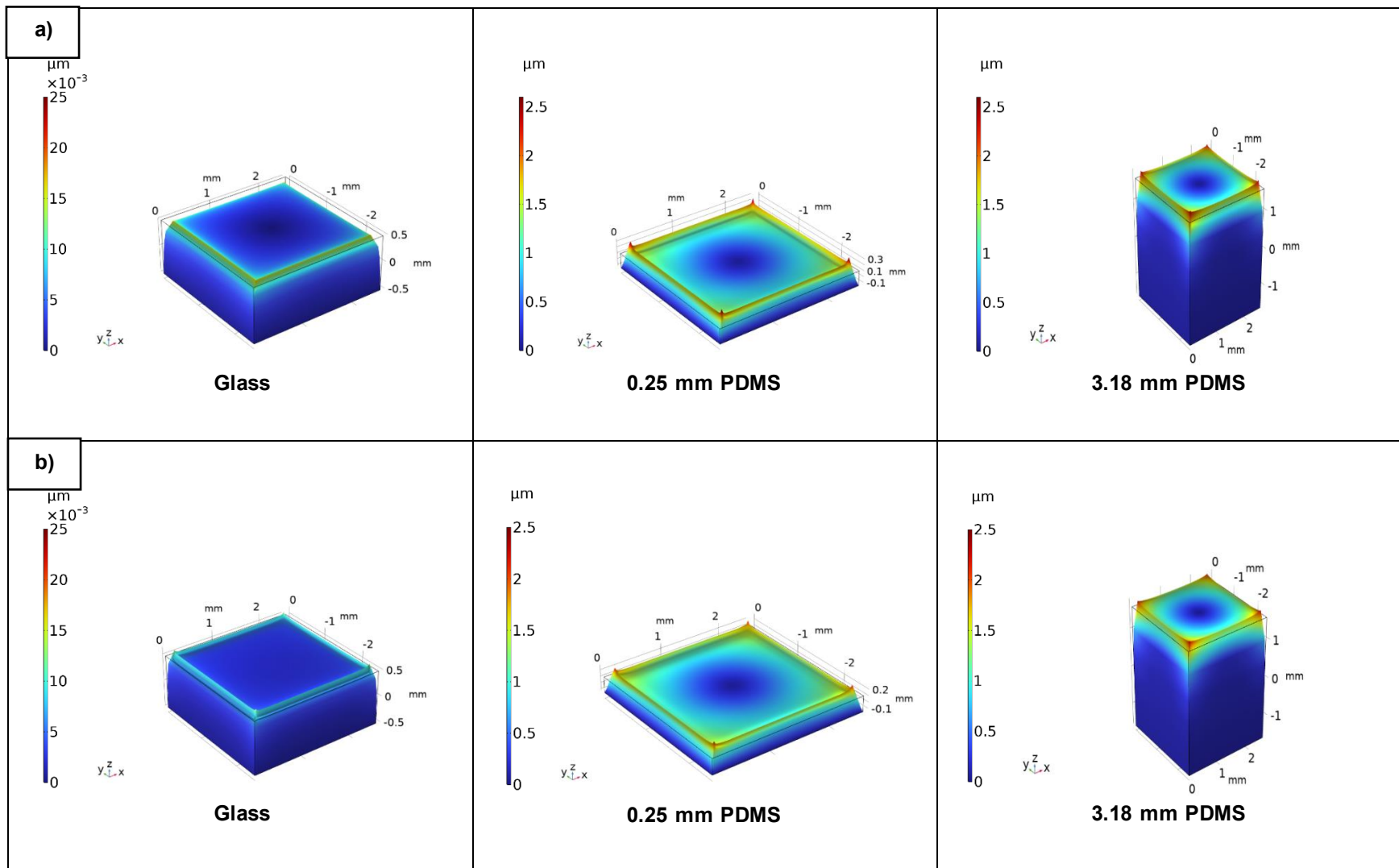
Figure 4: Simulated deformations for post-deposition AuAg (a) and post-dealloying np-Au (b) states with representative substrate types of glass, 0.25 mm-thick PDMS and 3.18 mm-thick PDMS. Blue color represents zero deformation, while red represents the maximum value

These in-plane (horizontal) and vertical deformations may lead to buckling at the surface, evident from atomic force microscopy (AFM) studies (**Figure 5**). While the rigid glass substrates presented no signs of buckling, the compliant PDMS substrates exhibited an increase in buckling features, with the severity of the out-of-plane deformation escalating in tandem with the thickness of the PDMS.
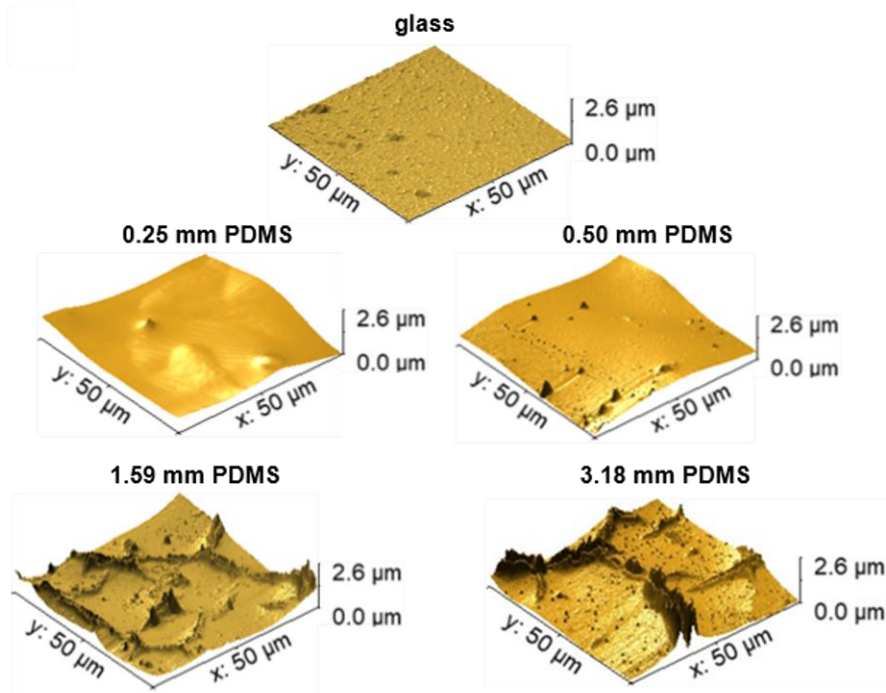

Figure 5: AFM topographies of the np-Au film surface on glass and PDMS of different thicknesses showing absence of buckling in np-Au/glass and variation of buckling in np-Au/PDMS. (Courtesy of Sadi Shahriar)

Figure 6 shows the elastic strain energies in the top metal layers and anchored PDMS substrates of different thicknesses (0.05 mm to 5 mm) before and after dealloying, as obtained from the simulations. **Figure 6a** also includes the strain energies in AuAg and np-Au on glass. A thermal strain corresponding to a stress of 100 MPa as mentioned above was applied to the metal layers to calculate the post-deposition strain energies. It was noted that the AuAg layer on glass initially possessed the greatest strain energy at 6.3×10^{-7} J, which was reduced to 1.5×10^{-7} J in np-Au post-dealloying (**Figure 6a**). For the AuAg film on PDMS with a 0.05 mm thickness, there was a

noticeable decline in strain energy from 2.9×10^{-8} J to 1.6×10^{-8} J once dealloyed, with both values decreasing with increasing PDMS thickness. Similarly, the strain energy measured for PDMS after deposition also decreased with increased PDMS thickness, from the highest value of 2.3×10^{-8} J at 0.05 mm to the lowest value of 2.1×10^{-9} J at 5 mm thickness (**Figure 6b**). The strain energy of the total film-PDMS system consistently dropped by a factor of ~1.3 after dealloying (**Figure 6b**).
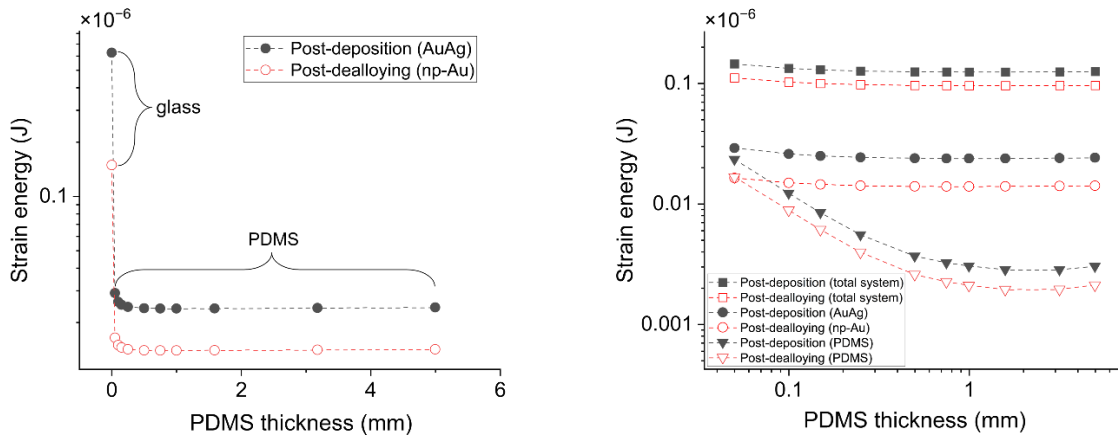

Figure 6: Post-deposition and post-dealloying variation in the elastic strain energy in (a) the AuAg and np-Au layers on glass and anchored PDMS of different thicknesses, and (b) the total strain energy in the entire film-substrate system, the AuAg and np-Au films, and the anchored PDMS.

To understand the spatial distribution of the strains in PDMS, **Figure 7** compares the strain meshes within the material, the strain being the local ε_{zz} strain component, sliced through the thickness of PDMS in the ZX plane for 0.25 mm and 3.18 mm thicknesses. This is crucial for understanding the mechanical behavior of the film-substrate system, particularly how strain is distributed through the material. It can be seen that major changes in the strain values occur at the thin film-PDMS interface at the top, and the effect vanishes closer to the bottom of PDMS, especially for the 3.18 mm-thick PDMS. Hence, it is important to consider the surface stiffness values of PDMS, and this is estimated by the effective elastic modulus of the PDMS.
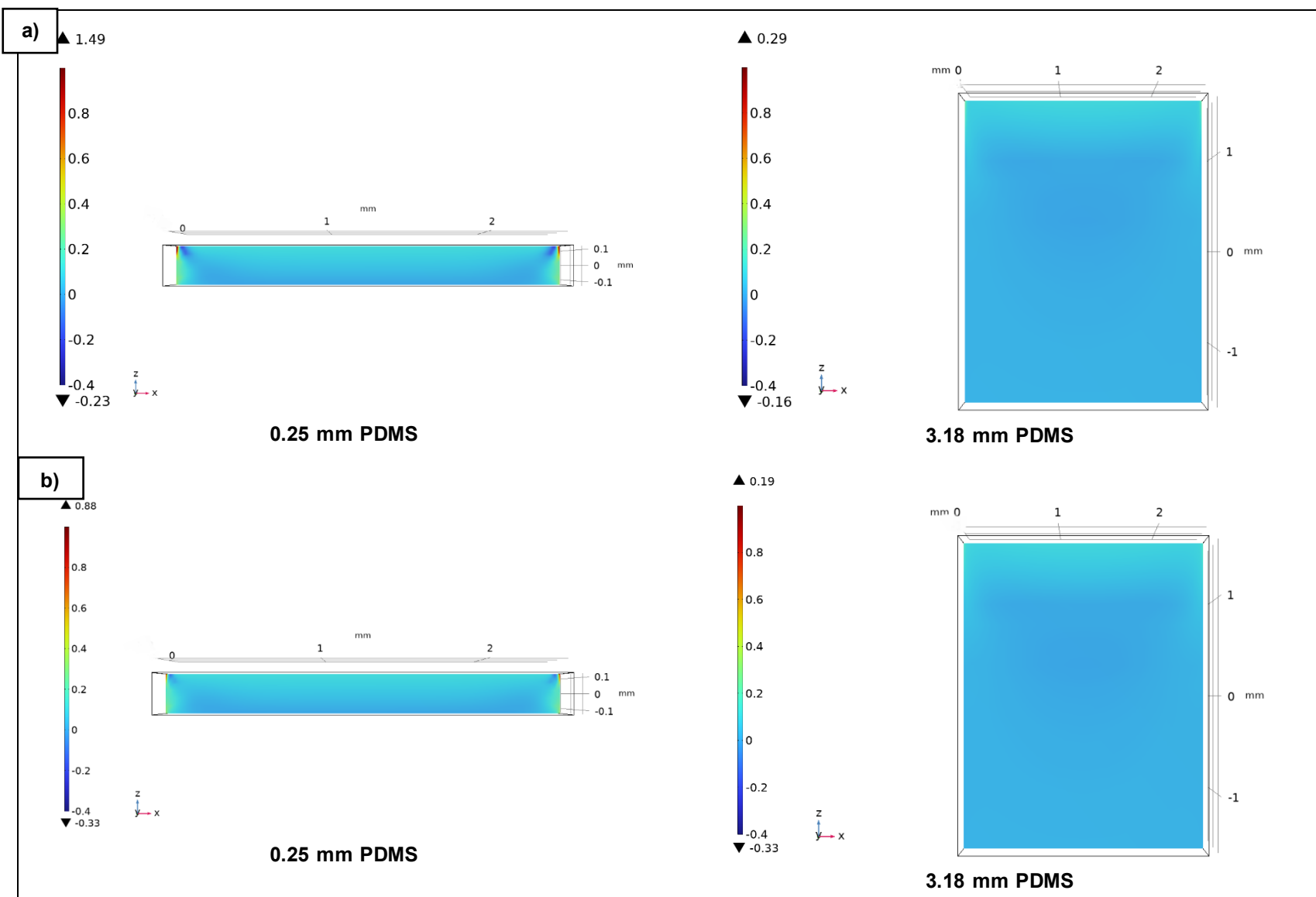
Figure 7: Strain in the Z-axis of post-deposition AuAg (a) and post-dealloying np-Au (b) states, sliced in the ZX plane for 0.25 mm and 3.18 mm PDMS thicknesses

Figure 8 shows the variation in the effective elastic modulus of the anchored PDMS substrates for different thicknesses (0.001 mm to 5 mm) as defined by Equation 1. There is a consistent decrease in the modulus with increasing PDMS thickness. It is important to note that at the minimum PDMS thickness of 0.01 mm, the modulus significantly surpasses that of glass, approximately 70 GPa [40] by Equation 1, since the simulations and the equation modeled the PDMS as being anchored to an infinitely rigid material. Experimentally, the maximum effective modulus of PDMS should not exceed 70 GPa and should only reach this value when the PDMS thickness approaches zero.
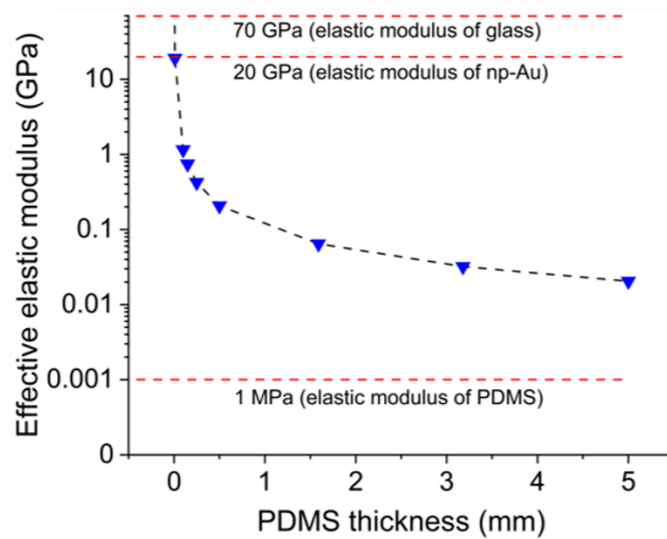

Figure 8: Effective elastic modulus of the PDMS substrate at the free surface as a function of the PDMS thickness. The black dashed line is a visual guide only.

The difference in the surface stiffness experienced by the metal thin film deposited on rigid glass versus compliant PDMS (different thicknesses within PDMS as well) with elastic moduli of ~70GPa and ~1 MPa [37] influences the morphological differences observed between np-Au/glass and np-Au/PDMS/glass configurations. Given that the PDMS substrate is anchored onto a glass slide, the thickness of the PDMS notably affects the effective elastic modulus of the

substrate, as demonstrated in **Figure 4**. The elastic mismatch between the film and substrate is quantified by the Dundurs' parameters, α and β [41], [42], which are defined as:

$$\alpha = \frac{\bar{E}_f - \bar{E}_s}{\bar{E}_f + \bar{E}_s}, \quad \beta = \frac{\bar{E}_f f(v_s) - \bar{E}_s f(v_f)}{\bar{E}_f + \bar{E}_s} \tag{5}$$

where the subscripts f and s respectively correspond to the film and substrate, $\bar{E} = E/(1 - v^2)$ and $f(v) = (1 - 2v)/[2(1 - v)]$ for the plane strain condition, E is the elastic modulus, and v is Poisson's ratio. According to Equation 5, α will be positive when the film is stiffer than the substrate, $E_f > E_s$, as is the case with np-Au/PDMS, and negative for np-Au/glass systems. This inversion in Dundurs' parameters, indicative of a shift from a compliant substrate to a rigid one, is expected to alter the primary mode of morphological evolution, consistent with the experimental outcomes of this investigation.

Post-deposition and post-dealloying stresses lead to the formation of cracks, while substrate stiffness significantly influences the distribution of these cracks and the overall film morphology. **Figure 9** shows top-view scanning electron microscope (SEM) images of np-Au thin films on glass and PDMS of varying thickness, at different magnifications, and they show a clear substrate stiffness-dependent variation in crack patterns. Macroscopic cracks become more prominent in np-Au/PDMS films after dealloying. In contrast, macroscopic cracks in np-Au/glass films appear at a smaller length scale than those in np-Au/PDMS films, and the patterns of the cracks differ. Microscopic cracks in np-Au/glass films are uniformly distributed, whereas in np-Au/PDMS films, they tend to form in a hierarchical pattern within islands, particularly on thicker substrates.
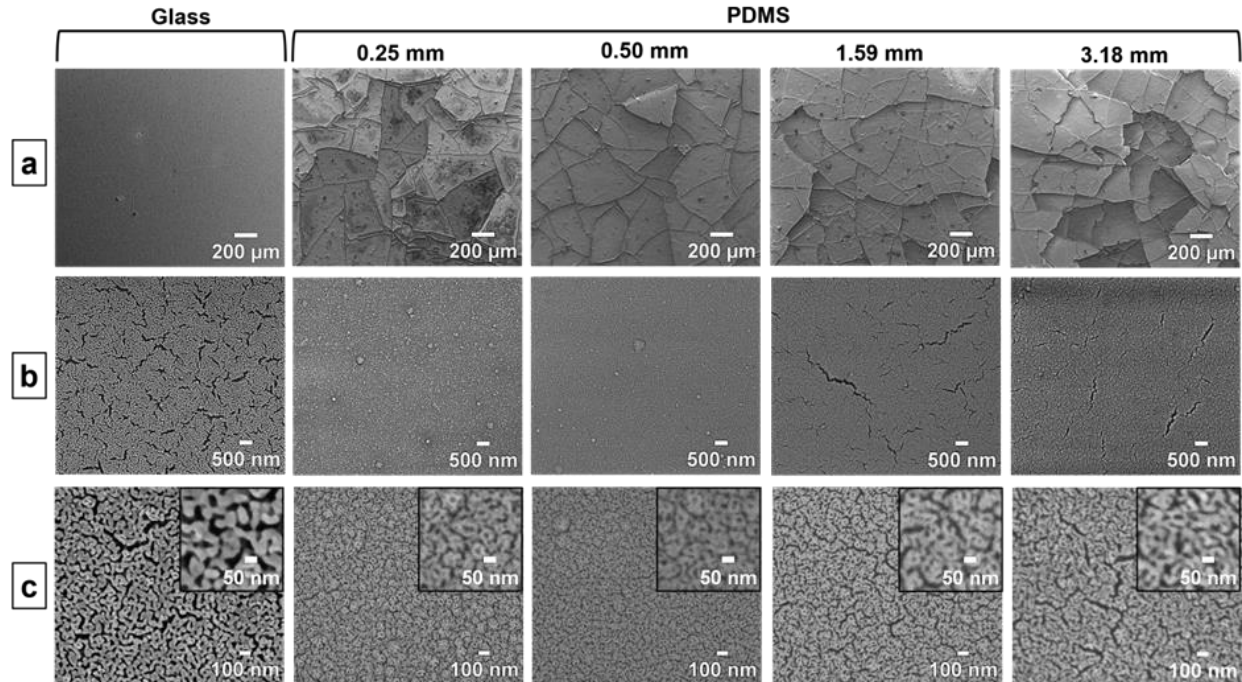
Figure 9: Top-view SEM images of (a) macroscopic cracks at 150X, (b) microscopic cracks at 35kX, and (c) ligaments and pores at 150kX magnifications in the np-Au thin films on glass and PDMS of varying thickness. (Courtesy of Sadi Shahriar)

It is important to note that as the thickness of PDMS decreases, the film's cracking behavior starts to resemble that observed on glass, according to experimental observations. This transition likely occurs at a critical thickness threshold of 0.01 mm, where the effective elastic modulus of PDMS surpasses that of np-Au, as indicated by the dashed red line at 20 GPa in **Figure 8**. Consequently, there is a reversal in the sign of Dundurs' parameter α from positive to negative (as defined in Equation 5), signifying a shift toward the behavior characteristic of a thin film on a stiffer substrate. However, despite these findings, np-Au films on the thinnest PDMS substrates tested (0.25 mm and 0.50 mm) did not display the crack pattern typically seen in np-Au/glass films. This discrepancy is likely due to the fact that, at these reduced thicknesses, PDMS maintains a significantly higher compliance than glass, and therefore, the behavior analogous to that of np-Au/glass is not expected.

Initially, the simulation efforts aimed to model the np-Au thin film at the scale of an individual crack and even attempted multiple crack scenarios, intending to directly capture the experimental conditions observed in the np-Au/PDMS system. However, this approach quickly proved to be problematic, resulting in artifactual outcomes quite different from both experimental observations and anticipated mechanical behaviors. The granularity required to accurately capture crack-scale phenomena introduced significant computational challenges and uncertainties, particularly in terms of aspect ratios of the film stack vs PDMS and having enough mesh elements with reasonable degrees of freedom.

Hence, instead of attempting to simulate conditions at the scale of individual cracks, the simulation focus shifted towards a more holistic approach. By analyzing the strain energies and deformations across the system, the behavior of the thin film and its interaction with substrates is predicted more abstractly, yet effectively. This method allowed to circumvent the limitations imposed by direct crack-scale modeling, offering a broader perspective on the material's response under various conditions.

This methodological adjustment underscores the adaptability required in simulation-based research and highlights the importance of selecting appropriate scales and parameters to align with the study's objectives and the limitations of available tools.

4. CONCLUSION

With this thesis, using FEA simulations and key experimental findings, the significant role of substrate compliance denoted as "effective elastic modulus", and how variations in PDMS thickness distinctly influence strain energies and deformations is explored. Simulations have been pivotal in corroborating experimental findings, providing deeper insights into the mechanical responses of np-Au films under different substrate conditions.

The absence of cracks in as-deposited films on glass starkly contrasts with the widespread cracking observed across all scales post-dealloying, a phenomenon not present in films on PDMS substrates. Further, the simulation outcomes have elucidated the transition in cracking patterns from glass to PDMS substrates based on the effective elastic modulus, where macroscopic cracks evolve to form discrete islands with decreasing widths as PDMS thickness increases. This trend was mirrored in the microscopic cracks, which intensified with PDMS thickness, a finding substantiated by the simulations that highlighted the increasing deformation and distribution of strain energies within the thin films.

In conclusion, the study demonstrates that the engineering of morphology in np-Au thin films across different scales is feasible through careful manipulation of compliant substrate thickness, as supported by both experimental and simulation findings. The potential to create nearly crack-free np-Au films on PDMS by analyzing the energies and deformations presents a significant advancement for the application of np-Au functional coatings. The simulation approach, with supporting experimental work not only enhances our understanding of np-Au film behavior across different substrates but also opens new avenues for designing advanced materials for flexible and wearable technology applications. This thesis lays a foundational step towards leveraging simulation tools for predictive modeling in materials science, offering pathways for future research to refine and expand upon these initial insights.

References

[1] E. Acosta, "Thin Films/Properties and Applications," in *Thin Films*, IntechOpen, 2021. doi: 10.5772/intechopen.95527.

[2] S. Rout *et al.*, "Nanoporous gold nanoleaf as tunable metamaterial," *Sci. Rep.*, vol. 11, no. 1, Art. no. 1, Jan. 2021, doi: 10.1038/s41598-021-81128-4.

[3] "Nanomaterials | Free Full-Text | Hybrid Nanocomposite Thin Films for Photovoltaic Applications: A Review." Accessed: Feb. 12, 2024. [Online]. Available: https://www.mdpi.com/2079-4991/11/5/1117

[4] H. J. Griesser, *Thin Film Coatings for Biomaterials and Biomedical Applications*. Woodhead Publishing, 2016.

[5] L. Wang, K. Jiang, and G. Shen, "Wearable, Implantable, and Interventional Medical Devices Based on Smart Electronic Skins," *Adv. Mater. Technol.*, vol. 6, no. 6, p. 2100107, 2021, doi: 10.1002/admt.202100107.

[6] M. F. Silva *et al.*, "NBI Optical Filters in Minimally Invasive Medical Devices," *IEEE J. Sel. Top. Quantum Electron.*, vol. 22, no. 4, pp. 165–171, Jul. 2016, doi: 10.1109/JSTQE.2016.2514709.

[7] M. Mozafari, A. Ramedani, Y. N. Zhang, and D. K. Mills, "8 - Thin films for tissue engineering applications," in *Thin Film Coatings for Biomaterials and Biomedical Applications*, H. J. Griesser, Ed., Woodhead Publishing, 2016, pp. 167–195. doi: 10.1016/B978-1-78242-453-6.00008-0.

[8] L. Vannozzi, V. Iacovacci, A. Menciassi, and L. Ricotti, "Nanocomposite thin films for triggerable drug delivery," *Expert Opin. Drug Deliv.*, vol. 15, no. 5, pp. 509–522, May 2018, doi: 10.1080/17425247.2018.1451512.

[9] S. Karki, H. Kim, S.-J. Na, D. Shin, K. Jo, and J. Lee, "Thin films as an emerging platform for drug delivery," *Asian J. Pharm. Sci.*, vol. 11, no. 5, pp. 559–574, Oct. 2016, doi: 10.1016/j.ajps.2016.05.004.

[10] E. Torres Dominguez, P. Nguyen, A. Hylen, M. R. Maschmann, A. Mustapha, and H. K. Hunt, "Design and characterization of mechanically stable, nanoporous TiO2 thin film antimicrobial coatings for food contact surfaces," *Mater. Chem. Phys.*, vol. 251, p. 123001, Sep. 2020, doi: 10.1016/j.matchemphys.2020.123001.

[11] O. O. Abegunde *et al.*, "Overview of thin film deposition techniques," *AIMS Mater. Sci.*, vol. 6, no. 2, pp. 174–199, 2019, doi: 10.3934/matersci.2019.2.174.

[12] H. Ichou, N. Arrousse, E. Berdimurodov, and N. Aliev, "Exploring the Advancements in Physical Vapor Deposition Coating: A Review," *J. Bio- Tribo-Corros.*, vol. 10, no. 1, p. 3, Nov. 2023, doi: 10.1007/s40735-023-00806-0.

[13] A. Baptista, F. Silva, J. Porteiro, J. Míguez, and G. Pinto, "Sputtering Physical Vapour Deposition (PVD) Coatings: A Critical Review on Process Improvement and Market Trend Demands," *Coatings*, vol. 8, no. 11, Art. no. 11, Nov. 2018, doi: 10.3390/coatings8110402.

[14] K. Seshan, *Handbook of Thin Film Deposition*. William Andrew, 2012.

[15] P. Bhattacharyya and S. Basu, "CVD Grown Materials for High Temperature Electronic Devices : A Review," *Trans. Indian Ceram. Soc.*, vol. 70, no. 1, pp. 1–9, Jan. 2011, doi: 10.1080/0371750X.2011.10600145.

[16] P. D. Dapkus, "Metalorganic Chemical Vapor Deposition," *Annu. Rev. Mater. Sci.*, vol. 12, no. 1, pp. 243–269, 1982, doi: 10.1146/annurev.ms.12.080182.001331.

[17] P. S. Alexopoulos and T. C. O'Sullivan, "Mechanical Properties of Thin Films," *Annu. Rev. Mater. Sci.*, vol. 20, no. 1, pp. 391–420, 1990, doi: 10.1146/annurev.ms.20.080190.002135.

[18] W. D. Nix, "Mechanical properties of thin films," *Metall. Trans. A*, vol. 20, no. 11, pp. 2217–2245, Nov. 1989, doi: 10.1007/BF02666659.

[19] M. D. Thouless, "Modeling the Development and Relaxation of Stresses in Films," *Annu. Rev. Mater. Sci.*, vol. 25, no. 1, pp. 69–96, 1995, doi: 10.1146/annurev.ms.25.080195.000441.

[20] C. J. Lee, J. Park, Y. Huh, and J. Yong Lee, "Temperature effect on the growth of carbon nanotubes using thermal chemical vapor deposition," *Chem. Phys. Lett.*, vol. 343, no. 1, pp. 33–38, Jul. 2001, doi: 10.1016/S0009-2614(01)00680-7.

[21] M. S. Kim *et al.*, "Effects of cooling rate and post-heat treatment on properties of ZnO thin films deposited by sol–gel method," *Appl. Surf. Sci.*, vol. 257, no. 21, pp. 9019–9023, Aug. 2011, doi: 10.1016/j.apsusc.2011.05.092.

[22] S. F. Lu, L. Ma, P. L. Dong, X. Zhou, and L. Li, "Effect of cooling rate on structure and magnetic properties of FePt thin films," *Mater. Res. Express*, vol. 6, no. 12, p. 126112, Dec. 2019, doi: 10.1088/2053-1591/ab5c74.

[23] G. Ye *et al.*, "Influence of post-deposition annealing on interfacial properties between GaN and ZrO2 grown by atomic layer deposition," *Appl. Phys. Lett.*, vol. 105, no. 15, p. 152104, Oct. 2014, doi: 10.1063/1.4898577.

[24] S. Naghdi, K. Y. Rhee, D. Hui, and S. J. Park, "A Review of Conductive Metal Nanomaterials as Conductive, Transparent, and Flexible Coatings, Thin Films, and Conductive Fillers: Different Deposition Methods and Applications," *Coatings*, vol. 8, no. 8, Art. no. 8, Aug. 2018, doi: 10.3390/coatings8080278.

[25] A. A. Talin *et al.*, "Tunable Electrical Conductivity in Metal-Organic Framework Thin-Film Devices," *Science*, vol. 343, no. 6166, pp. 66–69, Jan. 2014, doi: 10.1126/science.1246738.

[26] P. Á. Szilágyi, R. J. Westerwaal, R. van de Krol, H. Geerlings, and B. Dam, "Metal–organic framework thin films for protective coating of Pd-based optical hydrogen sensors," *J. Mater. Chem. C*, vol. 1, no. 48, pp. 8146–8155, Nov. 2013, doi: 10.1039/C3TC31749H.

[27] C. C. Mardare, M. Spiegel, A. Savan, and A. Ludwig, "Thermally Oxidized Mn–Co Thin Films as Protective Coatings for SOFC Interconnects," *J. Electrochem. Soc.*, vol. 156, no. 12, p. B1431, Oct. 2009, doi: 10.1149/1.3240597.

[28] E. Kalinina and E. Pikalova, "Opportunities, Challenges and Prospects for Electrodeposition of Thin-Film Functional Layers in Solid Oxide Fuel Cell Technology," *Materials*, vol. 14, no. 19, Art. no. 19, Jan. 2021, doi: 10.3390/ma14195584.

[29] E. Seker, M. L. Reed, and M. R. Begley, "Nanoporous Gold: Fabrication, Characterization, and Applications," *Materials*, vol. 2, no. 4, pp. 2188–2215, Dec. 2009, doi: 10.3390/ma2042188.

[30] G. Wittstock *et al.*, "Nanoporous Gold: From Structure Evolution to Functional Properties in Catalysis and Electrochemistry," *Chem. Rev.*, May 2023, doi: 10.1021/acs.chemrev.2c00751.

[31] Y. K. Chen-Wiegart, S. Wang, I. McNulty, and D. C. Dunand, "Effect of Ag–Au composition and acid concentration on dealloying front velocity and cracking during nanoporous gold formation," *Acta Mater.*, vol. 61, no. 15, pp. 5561–5570, Sep. 2013, doi: 10.1016/j.actamat.2013.05.039.

[32] P. Daggumati, O. Kurtulus, C. A. R. Chapman, D. Dimlioglu, and E. Seker, "Microfabrication of nanoporous gold patterns for cell-material interaction studies," *J. Vis. Exp. JoVE*, no. 77, p. e50678, Jul. 2013, doi: 10.3791/50678.

[33] L. Sabat and C. K. Kundu, "History of Finite Element Method: A Review," in *Recent Developments in Sustainable Infrastructure*, B. B. Das, S. Barbhuiya, R. Gupta, and P. Saha, Eds., in Lecture Notes in Civil Engineering. Singapore: Springer, 2021, pp. 395–404. doi: 10.1007/978-981-15-4577-1_32.

[34] S. A. Hollingsworth and R. O. Dror, "Molecular dynamics simulation for all," *Neuron*, vol. 99, no. 6, pp. 1129–1143, Sep. 2018, doi: 10.1016/j.neuron.2018.08.011.

[35] E. Seker *et al.*, "The effects of post-fabrication annealing on the mechanical properties of freestanding nanoporous gold structures," *Acta Mater.*, vol. 55, no. 14, pp. 4593–4602, Aug. 2007, doi: 10.1016/j.actamat.2007.03.018.

[36] E. Seker, M. L. Reed, and M. R. Begley, "A thermal treatment approach to reduce microscale void formation in blanket nanoporous gold films," *Scr. Mater.*, vol. 60, no. 6, pp. 435–438, Mar. 2009, doi: 10.1016/j.scriptamat.2008.11.027.

[37] R. Seghir and S. Arscott, "Extended PDMS stiffness range for flexible systems," *Sens. Actuators Phys.*, vol. 230, pp. 33–39, Jul. 2015, doi: 10.1016/j.sna.2015.04.011.

[38] U. Holzwarth and H. Stamm, "Mechanical and thermomechanical properties of commercially pure chromium and chromium alloys," *J. Nucl. Mater.*, vol. 300, no. 2, pp. 161–177, Feb. 2002, doi: 10.1016/S0022-3115(01)00745-0.

[39] P. F. Kelly, *Properties of Materials*. CRC Press, 2014.

[40] "Materials and the Environment - 2nd Edition | Elsevier Shop." Accessed: Feb. 27, 2024. [Online]. Available: https://shop.elsevier.com/books/materials-and-the-environment/ashby/978-0-12-385971-6

[41] M. D. Thouless, Z. Li, N. J. Douville, and S. Takayama, "Periodic cracking of films supported on compliant substrates," *J. Mech. Phys. Solids*, vol. 59, no. 9, pp. 1927–1937, Sep. 2011, doi: 10.1016/j.jmps.2011.04.009.

[42] S. S. Chakravarthy, E. H. Jordan, and W. K. S. Chiu, "Thin film and substrate cracking under the influence of externally applied loads," *Eng. Fract. Mech.*, vol. 72, no. 8, pp. 1286–1298, May 2005, doi: 10.1016/j.engfracmech.2004.09.006.

Appendix

This appendix provides detailed visual representations of the simulation methodology employed in the research. The images included depict the sequence of simulations conducted using COMSOL Multiphysics software (Version 6.0). Each figure is accompanied by a brief description to explain the context within which the simulation was performed.

Step 1 – Create structure geometry

PDMS of thicknesses described previously were created and the adhesion layers of chromium and gold, followed by AuAg or np-Au, were added on top of the PDMS.
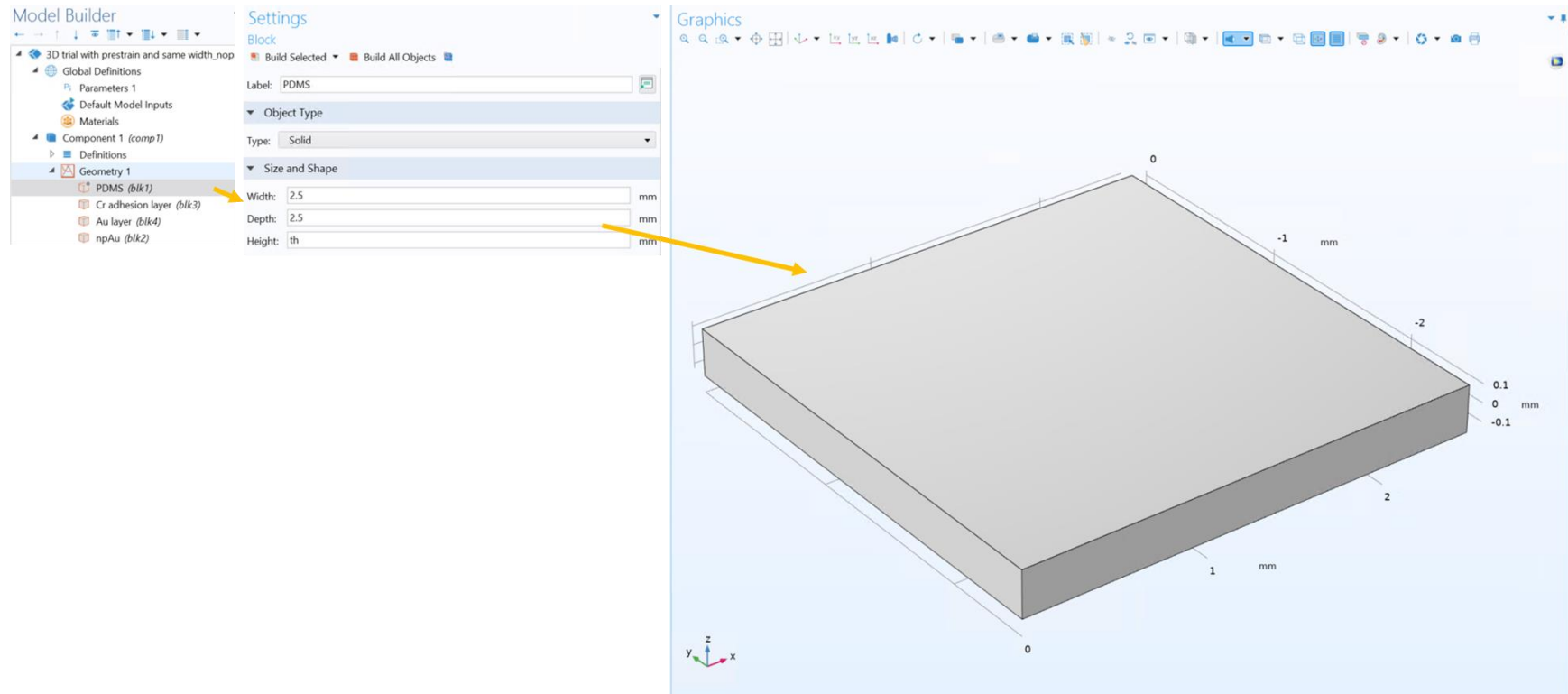
Figure A1: Steps involved in creating the thin film-substrate geometry.

Step 2 – Enter material properties

The appropriate layer/domain for each material was selected with the corresponding material properties. Note – For PDMS and np-Au/AuAg, new materials were created, whereas for Cr and Au, standard material properties from material library were selected.
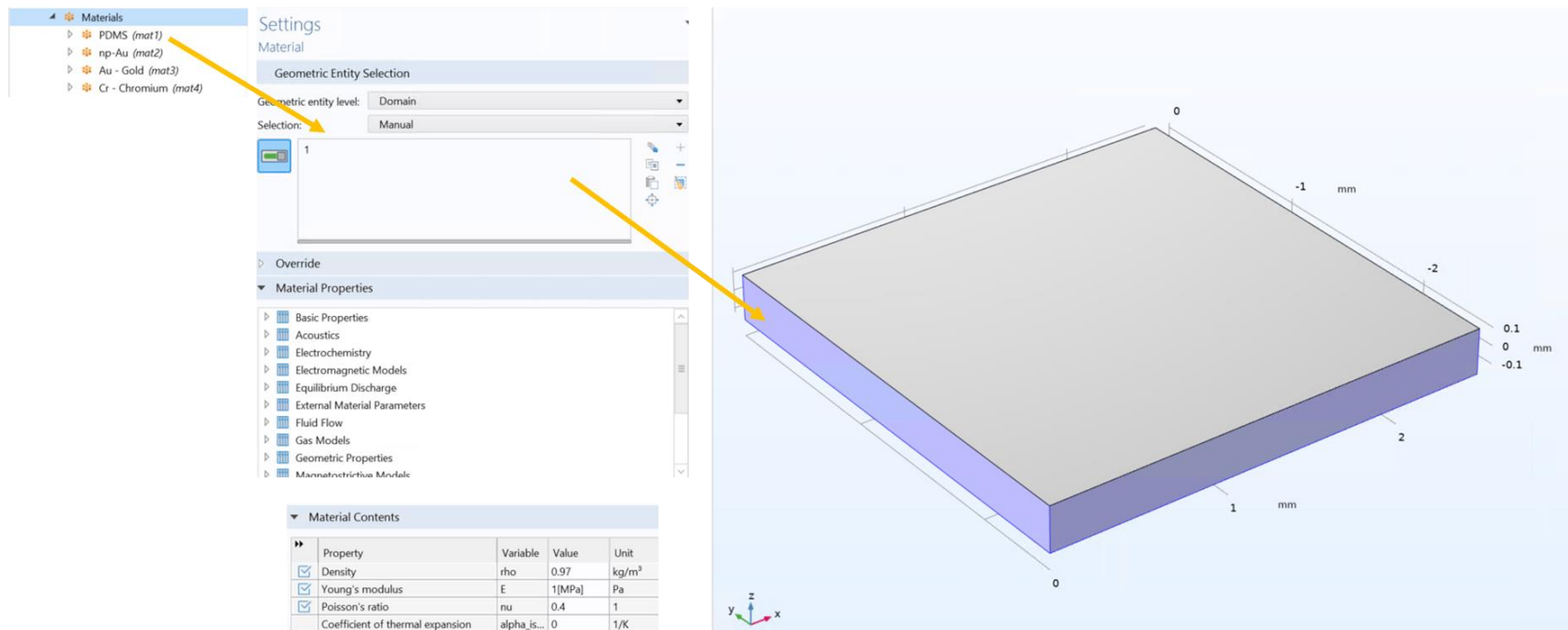
Figure A2: Steps involved in applying material properties to thin film layers.

Step 3 – Define boundary and loading conditions

First, the bottom surface of PDMS was given a Fixed Constraint condition. The thin film/adhesion layers were given a thermal expansion condition with temperature difference calculated using Equation 3.
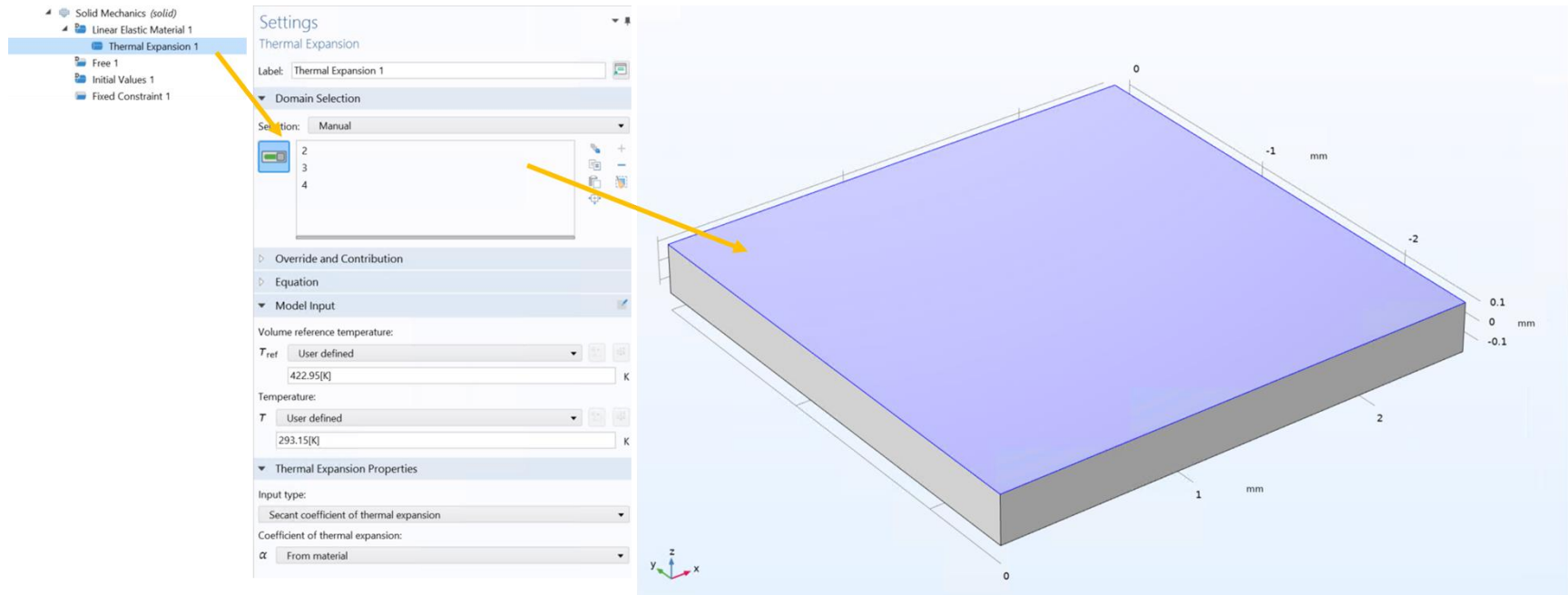
Figure A3: Steps involved in defining the boundary and loading conditions.

Step 4 – Create the mesh

Within Mesh menu, maximum and minimum element sizes for overall simulation were defined first. A free quad mesh was then applied to the np-Au/AuAg layer and the same mesh was swept for all layers, with varying elements through thickness for each layer.
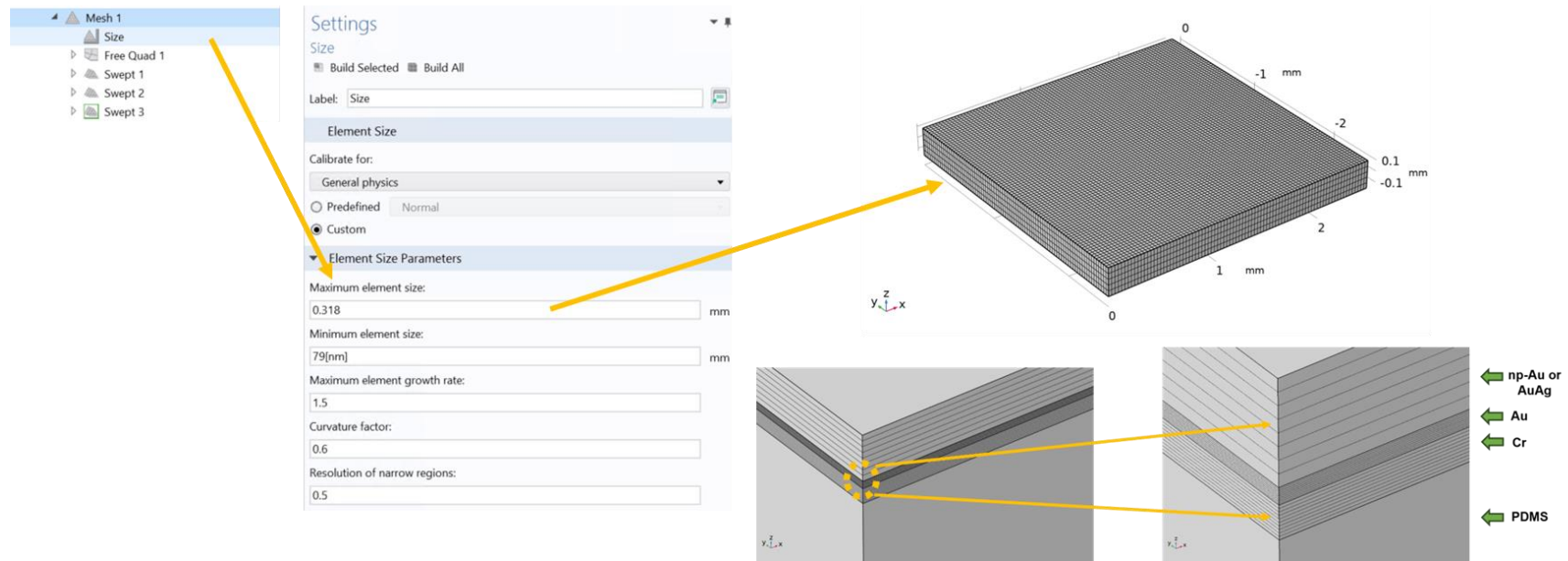

Figure A4: Steps involved in creating the mesh, with a representative mesh image.**10**

Step 5 – Define simulation parameters

Parametric sweep option was selected here to find the solution to a sequence of stationary or time-dependent problems that arise when parameters-of-interest was varied. Here, the parameter-of interest is the PDMS thickness, denoted by 'th', which was initially defined in the Global definitions tab. PDMS thicknesses of interest were employed in the Parametric sweep dialogue box.
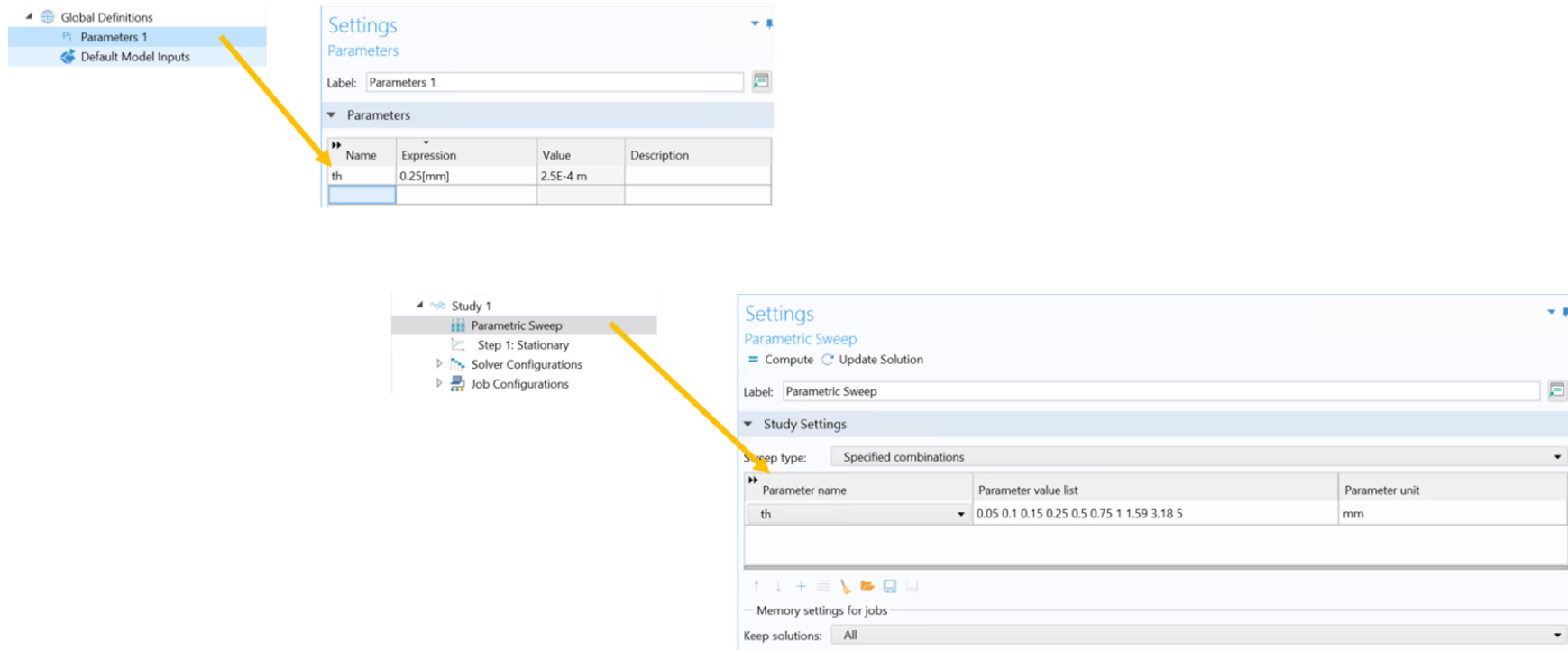
Figure A5: Steps involved in creating parametric sweep study.

Step 6 – Results

Appropriate plot groups of interest were selected (e.g., Displacement output shown below). By varying the 'th' parameter for different PDMS thickness, corresponding deformed meshes were obtained to extract output parameters.
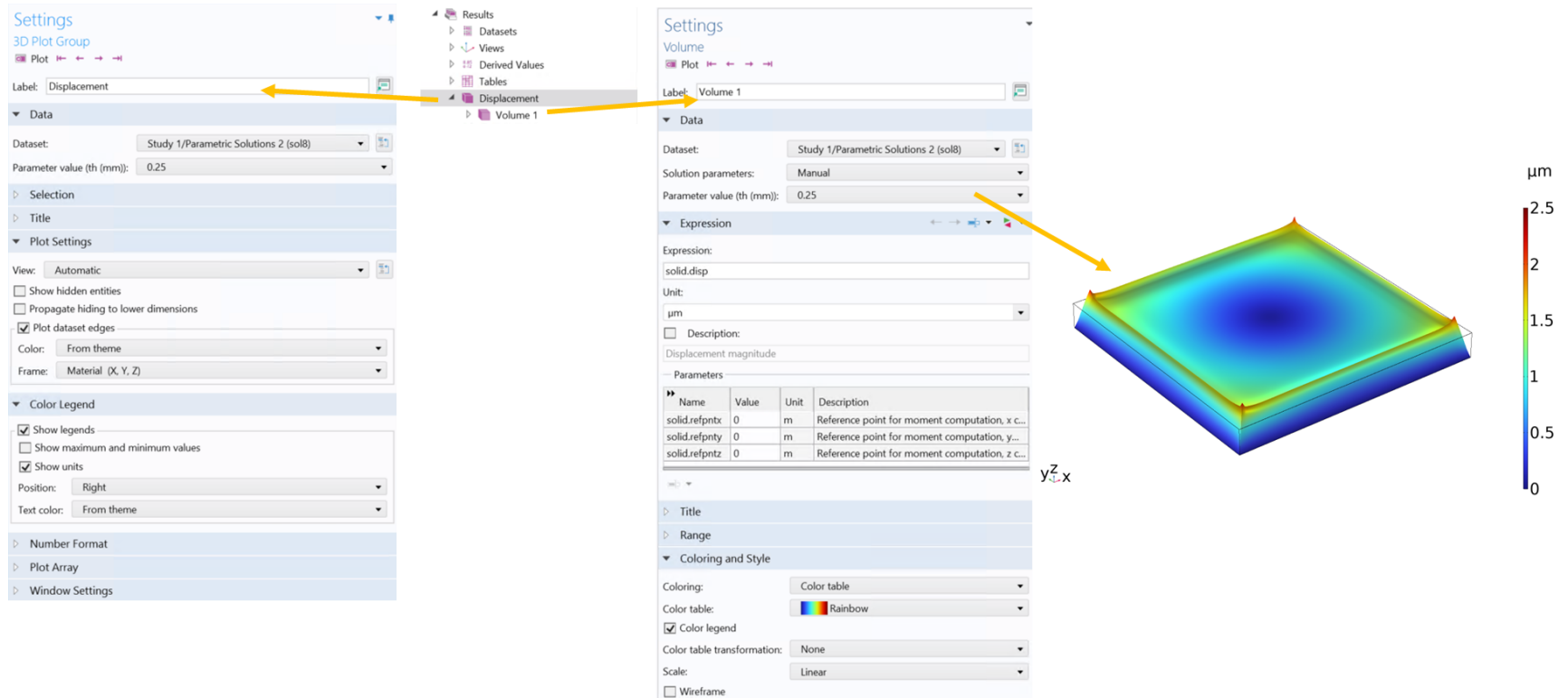

Figure A6: Displacement plot group information and representative displacement heatmap.